RSC Advances

ROYAL SOCIETY OF CHEMISTRY

PAPER

View Article Online
View Journal | View Issue

Cite this: *RSC Adv.*, 2024, **14**, 31979

Development and optimization of a sustainable polyoxometalate-kaolinite-based catalyst for efficient desulfurization of model and real fuel using Box–Behnken design

Hamna Khalid,[a] Arsheen Umar,[a] Muhammad Shahid Nazir,[a] Muhammad Asim Farid,[b] Zulfiqar Ali,[a] Asif Mahmood,[c] Waheed Al-Masry,[c] Chan Ho Park,[d] Toheed Akhter *[d] and Sadaf Ul Hassan*[a]

The oxidative desulfurization of dibenzothiophene in model and real fuel has been investigated by developing an environmentally sustainable catalyst $H_4SiW_{12}O_{40}$@f-kaolinite. The catalyst was synthesized by modifying kaolinite clay with (3-aminopropyl)triethoxysilane (f-kaolinite) followed by immobilizing silicotungstic acid hydrate ($H_4SiW_{12}O_{40}$) onto its surface. The successful synthesis of the catalyst was characterized by Fourier transform infrared spectroscopy, Raman spectroscopy, UV-visible spectroscopy, X-ray diffraction, energy-dispersive X-ray spectroscopy, and scanning electron microscopy. The influence of variables *i.e.*, catalyst dosage, temperature, and oxidant concentration on the conversion of dibenzothiophene was optimized by Box–Behnken design. The highest sulfur reduction (from 1000 to 78.3 ppm, with a conversion rate of 92.17%) was achieved at 70 °C, using a catalyst dosage of 70 mg and 8 mL of H_2O_2 in a model fuel. ANOVA analysis indicated that the quadratic model ($R^2 = 0.99$) was well-fitted for dibenzothiophene conversion, with a p-value of 0.2302 suggesting no statistically significant lack of fit compared to pure error. Furthermore, the $H_4SiW_{12}O_{40}$@f-kaolinite demonstrated a reduction of dibenzothiophene concentration from 354 ppm to 224 ppm in a real fuel oil sample. The heterogeneous nanocatalyst showed remarkable stability, maintaining its elemental structure after five cycles without significant efficiency loss, promoting environmental sustainability.

Received 25th August 2024
Accepted 3rd October 2024

DOI: 10.1039/d4ra06156j

rsc.li/rsc-advances

1 Introduction

In today's global landscape, energy production stands as a paramount concern deeply intertwined with economic activities and consumption patterns. Fossil fuels, notably petroleum, hold a commanding presence in the energy sector, constituting over 82% of the world's energy supply. Among these, crude oil, comprising diverse organic compounds, emerges as the primary source, particularly for transportation fuels.[1,2] The sulfur content in crude oil, varying from less than 0.1% to over 5%, holds significant importance as it determines the classification of crude oil as 'sweet' or 'sour'.[3] Sulfur compounds, both inorganic and organic, are prevalent in crude oil.[4,5] These compounds, which encompass mercaptans, sulfides, thiophenes, and polysulfides, contribute to harmful emissions such as sulfur dioxide (SO_2) and sulfate particulate matter, exacerbating issues like acid rain. Moreover, they pose corrosion risks for catalysts and engines, thus warranting effective desulfurization strategies.[6–9]

In recent years, heightened attention has been directed towards achieving comprehensive sulfur removal from fuel oils, propelled by ever-stringent environmental regulations. Oxidative desulfurization (ODS) stands out as a key method due to its effectiveness at relatively low reaction temperatures.[10,11] This technique promotes the sequential oxidation of sulfur-containing compounds in fuel feedstocks, starting with the formation of sulfoxides and progressing to sulfones.[12,13] During the ODS process, oxidizing agents introduce reactive oxygen species to sulfur compounds, leading to the preparation of sulfones. This transformation significantly alters the polarity and weakens the carbon-sulfur (C–S) bonds, making sulfones more easily separable from hydrocarbons (oil) and facilitating further processing and use.[2,5]

Polyoxometalates (POMs) are clusters comprising metal and oxygen atoms, characterized by diverse structures and unique electronic properties.[14,15] Their versatility finds applications

[a]*Department of Chemistry, COMSATS University Islamabad, Lahore Campus, Defence Road, Off Raiwind Road, Lahore 54000, Pakistan*

[b]*Department of Chemistry, Division of Science and Technology, University of Education, 54770 Lahore, Pakistan*

[c]*Department of Chemical Engineering, College of Engineering, King Saud University, Riyadh, 11421, Kingdom of Saudi Arabia*

[d]*Department of Chemical and Biological Engineering, Gachon University, Seongnam 13120, Republic of Korea*

across various fields, including magnetism, electricity, photochemistry, and pharmaceuticals. Notably, POMs have emerged as favored catalysts for ODS due to their distinct advantages over alternative catalysts. These advantages include remarkable selectivity, thermal stability, and the capacity to modify acidity and redox properties to suit specific requirements.[16] However, the catalytic efficacy of POMs is often constrained by their limited surface area, typically below 10 $m^2\ g^{-1}$, and challenges associated with their separation from reaction mixtures.[17] To overcome these limitations and enhance both surface area and recyclability, various strategies have been implemented. These include encapsulation with a support material, modification, and nano structuring.[18–20] Consequently, POMs are commonly integrated into structured materials such as kaolinite clay. This integration not only increases their surface area but also facilitates improved accessibility to the active sites of POMs for reactants.[21]

Kaolinite, a naturally occurring clay, exhibits a 1 : 1 dioctahedral layered structure, with an ideal chemical composition represented as $Al_4Si_4O_{10}(OH)_8$. This mineral possesses cation exchange capabilities and can accommodate certain organic molecules within its interlayer space.[22–24] Each kaolinite layer is composed of a single silica tetrahedral sheet paired with a single alumina octahedral sheet, resulting in a 1 : 1 structural arrangement. These individual layers are bound together within the crystal structure through O–H–O bonds, which form between the octahedral sheet of one layer and the tetrahedral sheet of the adjacent layer.[25–27] Kaolinite clays are esteemed as a crucial category of industrial minerals due to their remarkable physicochemical properties, non-toxic nature, cost-effectiveness, and widespread availability. These clays serve as versatile materials with applications across diverse fields, including geology, agriculture, catalysis, and various industrial processes such as ceramics, paper production, and paint manufacturing. In catalytic processes, both natural and modified forms of kaolinite clays play a pivotal role in organic reactions. These materials offer distinct advantages over traditional catalysts, including ease of manipulation, recyclability, cost-effectiveness, and the ability to regulate acidity levels through cation exchange, thereby aligning with the principles of "Green Chemistry".[28,29]

A wide variety of guest molecules *i.e.*, cetyltrimethylammonium bromide and triethoxy (octyl) silane,[30] functional ionic liquids,[31] aminosilyl, vinylsilyl groups,[32] polyethyleneimine,[33] and 3-amino propyl trimethoxy silane were reported in literature for the immobilization on the surface of kaolinite clay to manipulate and modify clay's inherent properties and enhance its application potential.[33] Organosilylation, a widely recognized technique, is employed for selectively modifying kaolinite clay by serving as a bridge layer between the intended guest molecule and the kaolinite surface.[34,35] The covalent bonding occurring between the organic functionalities of the organosilane and the hydroxyl groups of the kaolinite surface serves a dual purpose: fine-tuning the surface chemistry of the clay and ensuring secure immobilization of the organic components, thereby preventing their undesired release.[35–38]

In this study, we conducted the functionalization of kaolinite clay (f-kaolinite) followed by the immobilization of polyoxometalates (POMs) on the surface of the functionalized kaolinite. Functionalization with APTES introduces amine groups that significantly improve the dispersion of POMs, leading to an increased number of accessible active sites. The strong interaction between POMs and the functionalized kaolinite ensures catalyst reusability with minimal loss of activity over multiple cycles. Moreover, the affordability of kaolinite and APTES makes this catalyst a cost-effective alternative to noble metal-based systems, further enhancing its practical application. Our aim was to develop a facile and environmentally sustainable catalyst for use in the oxidative desulfurization of dibenzothiophene in both model and real fuel samples.

Additionally, we employed response surface methodology to optimize key variables such as catalyst dosage, temperature, and oxidant concentration, which influence dibenzothiophene conversions. Our overarching goal is to develop a robust, efficient, and reusable catalyst by harnessing the synergistic interactions between versatile silicotungstic acid hydrate and widely available, reactive, and inexpensive clays, enabling effective oxidative desulfurization.

In summary, our research presents an efficient catalyst, "polyoxometalate-kaolinite," with parameters optimized through a Box–Behnken design approach. This catalyst addresses the need for sustainable desulfurization in both model and real fuel samples, offering a promising solution for enhancing catalytic efficiency, cost-effectiveness, and environmental sustainability in fuel desulfurization processes.

2 Materials and methods

2.1. Chemicals

Kaolinite clay, (3-aminopropyl) triethoxysilane (APTES), silicotungstic acid hydrate ($H_4SiW_{12}O_{40}$), acetic acid, ethanol, and hydrochloric acid were purchased from Sigma-Aldrich, and used without further purification. HPLC-grade water and acetonitrile used throughout the HPLC analysis were also purchased from Sigma-Aldrich.

2.2. Synthesis of APTES-functionalized kaolinite clay (f-kaolinite)

APTES-functionalized kaolinite clay was synthesized by adding 0.4 mL of APTES to a mixture of ethanol and water (6 : 4). A small quantity of acetic acid (2 mL) was then added to this solution to maintain the pH at 3.75. Subsequently, 2 g of kaolinite clay was added to the mixture, which was stirred for 2 hours. The resulting mixture was then dried for approximately 1 hour at a temperature of around 80 °C.

The functionalization of kaolinite with APTES is aimed at introducing positively charged amine groups, which strongly interact with the negatively charged polyoxometalate (POM) clusters through electrostatic interactions. This strong binding ensures the stable immobilization of $H_4SiW_{12}O_{40}$ on the

kaolinite surface, effectively preventing leaching during the oxidative desulfurization process.

2.3. Synthesis of $H_4SiW_{12}O_{40}$@f-kaolinite

The previously prepared f-kaolinite (160 mg) was dispersed in 12 mL of deionized water, and 1.2 mL of HCl was added to adjust the pH to 2. The mixture was stirred for 30 minutes, after which 160 mg of $H_4SiW_{12}O_{40}$ was added and stirred continuously for 6 hours. The resulting mixture was then dried at 80 °C for approximately 1 hour.

2.4. Characterizations

Physicochemical characterization of the synthesized samples was performed using various techniques. Functional group identification was achieved through Fourier Transform Infrared (FT-IR) spectroscopy on a Thermo Nicolet 6700 instrument. The analysis covered a wavenumber range of 4000–400 cm^{-1}. UV-visible spectroscopy was employed using a Shimadzu UV-2550 spectrophotometer to record spectra within the 200–800 nm range. Crystallographic phases of the samples were determined by powder X-ray diffraction (PXRD) utilizing a PANalytical x'Pert3 diffractometer with Cu Kα radiation. The analysis covered a 2θ range of 10–50°. Scanning Electron Microscopy (SEM) and energy-dispersive X-ray spectroscopy (EDX), performed on a Tescan Orsay Holding VEGA-3 LMU instrument, were used to investigate the morphology and elemental composition of the catalysts, respectively. High-performance liquid chromatography (HPLC) was conducted using HPLC-LC-2050 instrument, column temperature: 40 °C, a flow rate of 1 mL per minute, and mobile phase: acetonitrile and water in a 1 : 1 ratio. Each sample was analyzed for 20 minutes using a C18 column, and the UV wavelength employed was 254 nm.

3 Results and discussion

3.1. FTIR studies

The FT-IR spectrum (Fig. 1) of $H_4SiW_{12}O_{40}$ (heteropoly acid) exhibit three prominent absorption bands at 1014 cm^{-1}, 977 cm^{-1}, and 909 cm^{-1}, which can be attributed to W=O_d, Si–O_a, and W–O_b–W vibrations, respectively. In the spectrum of APTES, the absorption bands at 2971 cm^{-1} and 2879 cm^{-1} can be assigned to the asymmetric and symmetric stretching vibrations of CH_2 groups, respectively, indicating the presence of propyl chains within APTES. Additionally, peaks at 1607 cm^{-1} and 1387 cm^{-1} are linked to NH_2 scissoring vibrations, indicating the presence of NH_2 terminal groups in APTES. The FTIR spectrum of kaolinite revealed specific absorption bands at 3687 cm^{-1} and 3613 cm^{-1}, attributed to the hydroxyl groups. An absorption band at 1111 cm^{-1} was attributed to Si–O–Si deformation, while in-plane stretching of Si–O and O–H deformation vibrations of internal hydroxyl groups appeared at 983 cm^{-1} and 909 cm^{-1}, respectively. The identical positions of these peaks in both kaolinite and f-kaolinite indicate that the fundamental structure of kaolinite remained unchanged after APTES functionalization.

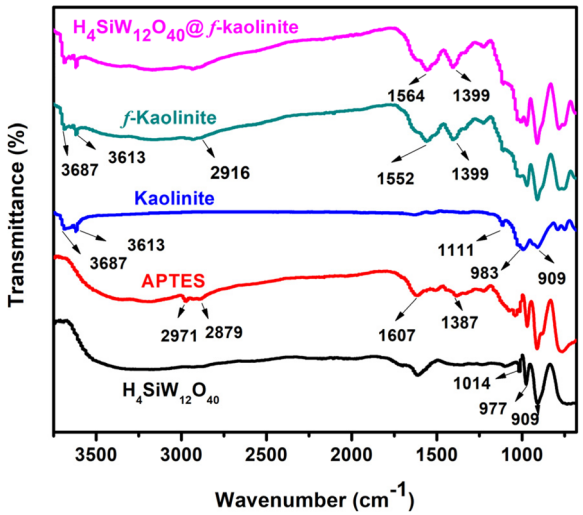

Fig. 1 FTIR spectra of $H_4SiW_{12}O_{40}$, APTES, kaolinite, f-kaolinite, and $H_4SiW_{12}O_{40}$@f-kaolinite.

However, in the kaolinite spectrum, new absorption bands emerged at 1552 cm^{-1}, 1399 cm^{-1}, and 2916 cm^{-1}, corresponding to the N–H and C–H vibrations in APTES. This finding confirms the successful functionalization of kaolinite with APTES. With further $H_4SiW_{12}O_{40}$ loading, the stretching vibration of the W=O bond in the $H_4SiW_{12}O_{40}$@f-kaolinite was obscured by the peak of the bending vibration of the hydroxyl group of Al–OH in kaolinite.

3.2. Raman analysis

The Raman spectra of $H_4SiW_{12}O_{40}$, kaolinite, f-kaolinite, and $H_4SiW_{12}O_{40}$@f-kaolinite were observed at an excitation wavelength of 457 nm (Fig. 2). The Raman spectra of $H_4SiW_{12}O_{40}$

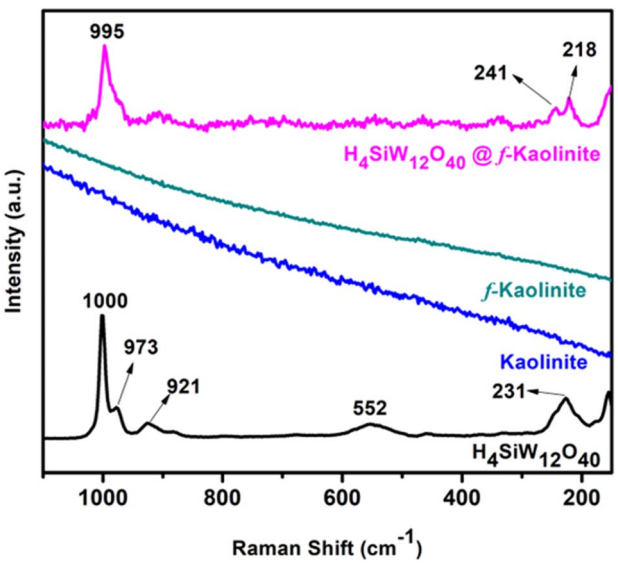

Fig. 2 Raman spectra of $H_4SiW_{12}O_{40}$, kaolinite, f-kaolinite, and $H_4SiW_{12}O_{40}$@f-kaolinite.

revealed the key bands associated with the Keggin anion. Prominent absorption features were detected in the range of 921 to 1000 cm^{-1}, corresponding to the symmetric vibrations of the W=O_d bonds. Additionally, a band at 973 cm^{-1} was identified with asymmetric stretching of the W=O bonds. Absorption bands in the range of 880 to 916 cm^{-1}, typically linked to the asymmetric stretching of the O–W–O bond, were observed to be too weak for clear detection. As $H_4SiW_{12}O_{40}$ contains silicon as the heteroatom, the band at 552 cm^{-1} refers to the stretching of the O–Si–O bond.[39] The kaolinite and f-kaolinite do not show any strong band in the 200–1100 cm^{-1} range at this wavelength. The synergistic interaction between $H_4SiW_{12}O_{40}$ and APTES-functionalized kaolinite leads to a broad peak at 995 cm^{-1}. The presence of these characteristic bands confirms the successful preparation and immobilization of $H_4SiW_{12}O_{40}$ on the functionalized kaolinite surface.

3.3. UV-Vis studies

UV-visible spectroscopy was employed to analyze the optical characteristics of the synthesized materials. The distinctive absorption bands in the 250–290 nm range were observed for kaolinite, f-kaolinite, and $H_4SiW_{12}O_{40}$@f-kaolinite, as shown in Fig. 3. The literature indicates that the absorption bands within the 200–480 nm arise from various electronic transitions. These include charge transfer, n → π* transition, pπ (O_t) → dπ* (W) transitions in W–O bonds, and n (O_b, c) → dπ* (W) transitions within the W–O–W bonds.[40]

The functionalization of kaolinite with APTES introduces organic moieties to the surface, which increases the absorbance of UV light. This results in a hyperchromic shift, leading to a more intense UV spectrum compared to pure kaolinite. Conversely, the immobilization of $H_4SiW_{12}O_{40}$ on f-kaolinite causes a hypsochromic shift. This shift to shorter wavelengths is due to the interaction between $H_4SiW_{12}O_{40}$ and f-kaolinite, which alters the electronic environment of the chromophores and changes the wavelength of maximum absorbance.

3.4. XRD studies

The XRD analysis was used to examine the structure of $H_4SiW_{12}O_{40}$, kaolinite, f-kaolinite, and $H_4SiW_{12}O_{40}$@f-kaolinite. The corresponding diffractograms are presented in Fig. 4. The XRD pattern of $H_4SiW_{12}O_{40}$ exhibits distinct peaks at 2θ values of 6.9, 8.2, and 29.46, indicating a highly crystalline structure and confirming the presence of the Keggin-type structure.[41] The XRD patterns of kaolinite and f-kaolinite show peaks at 2θ values of 12.32 and 24.79. The crystalline structure of kaolinite remains intact even after functionalization, suggesting no significant changes occurred during the process, except for a decrease in crystallinity. The XRD pattern of $H_4SiW_{12}O_{40}$@f-kaolinite demonstrates distinct peaks at 2θ values of 5.85, 9.43, and 12.66. Additionally, a broad region ranging from 17.6 to 33.16 indicates a loss of crystallinity in the structure upon the interaction of $H_4SiW_{12}O_{40}$ with f-kaolinite. This XRD data confirm the successful immobilization of $H_4SiW_{12}O_{40}$ on f-kaolinite and indicate that while the fundamental kaolinite structure remains intact, there is a reduction in crystallinity due to the interaction with $H_4SiW_{12}O_{40}$.

3.5. SEM and EDX studies

The morphology and elemental analysis of kaolinite and $H_4SiW_{12}O_{40}$@f-kaolinite were analyzed by SEM and EDX analysis as indicated in Fig. 5. The micrographs of untreated kaolinite powder exhibit the presence of pseudohexagonally arranged platelets in a stacked configuration, aggregated in disorderly form confirming the layered structure of clay. Concurrently, EDX analysis identifies the elemental composition, confirming the existence of aluminum, silicon, and oxygen constituents. The agglomeration of the particles was well observed in $H_4SiW_{12}O_{40}$@f-kaolinite, indicating the loss of crystallinity due to the synergistic interactions between the f-kaolinite and $H_4SiW_{12}O_{40}$, consistent with findings from XRD analysis. The distinctive peak of tungsten (21.62 weight%),

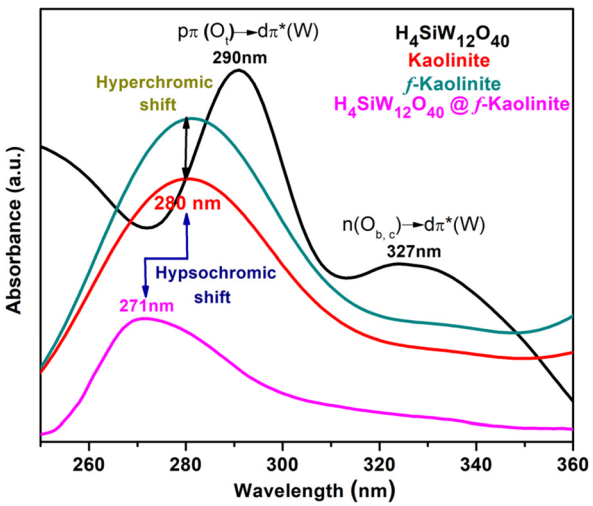

Fig. 3 UV spectra of $H_4SiW_{12}O_{40}$, kaolinite, f-kaolinite, and $H_4SiW_{12}O_{40}$@f-kaolinite (≈3.13 × 10^{-3} mM solution).

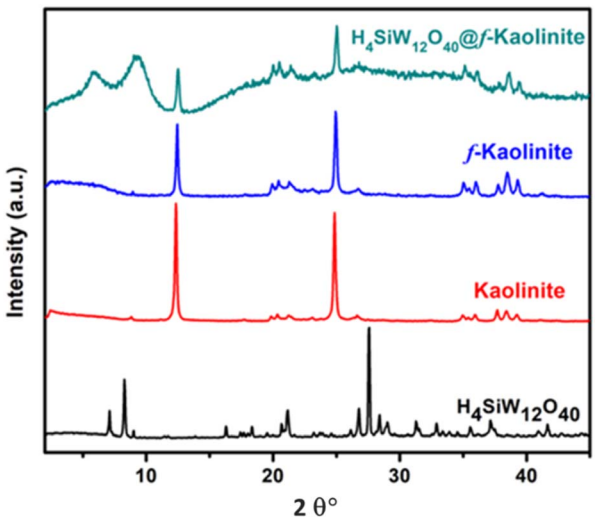

Fig. 4 XRD pattern of $H_4SiW_{12}O_{40}$, kaolinite, f-kaolinite, and $H_4SiW_{12}O_{40}$@f-kaolinite.

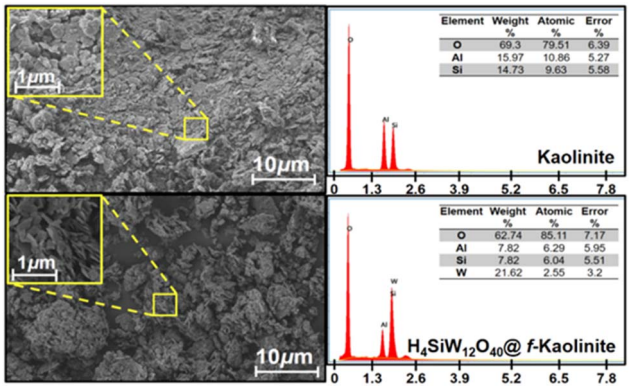

Fig. 5 SEM and EDX analysis of kaolinite and $H_4SiW_{12}O_{40}$@f-kaolinite.

oxygen, aluminum, and silicon confirmed the immobilization of $H_4SiW_{12}O_{40}$ on the surface of f-kaolinite resulting in the successful preparation of $H_4SiW_{12}O_{40}$@f-kaolinite.

3.6. Oxidative desulfurization of fuel oil

The ODS process was carried out using model fuel, H_2O_2 as the oxidant, acetonitrile as the extraction solvent, and $H_4SiW_{12}O_{40}$@f-kaolinite as the catalyst. Model fuel with a 1000 ppm concentration was prepared by dissolving dibenzothiophene (DBT) in *n*-hexane. In the ODS process, 25 mL of model fuel with 1000 ppm DBT, 0.1 grams of $H_4SiW_{12}O_{40}$@f-kaolinite, and 3 mL of hydrogen peroxide (30% by weight) were taken in a round-bottom flask and heated at 50 °C for 1 hour. After the reaction was completed, the upper supernatant was directly analyzed using HPLC. The conversion rate was calculated using the following formula (eqn (1)).

$$\text{Conversion}(\%) = \frac{C_i - C_0}{C_i} \times 100. \quad (1)$$

C_i represents the initial concentration of DBT and C_0 represents the concentration of dibenzothiophene after oxidation. The control ODS process with non-functionalized kaolinite, showed no detectable conversion, as kaolinite itself does not actively participate in desulfurization.

3.7. Optimization of ODS process parameters *via* BBD

Response Surface Methodology (RSM) was utilized to optimize and investigate the relationship between multiple independent variables and key parameter values, employing the Box–Behnken Design (BBD), aiming to effectively minimize both costs and duration. The experimental data was analyzed for effectiveness and accuracy using Design-Expert software (version 13). This methodology is commonly applied to study various phenomena including ODS.[42]

Three independent parameters, namely catalyst dosage (*A*), oxidant concentration (*B*), and temperature (*C*), were selected to optimize DBT conversion at three different levels: low (−1), medium (central point, 0), and high (+1). These independent variables and their corresponding levels are provided in Table 1. A 15-trial study was conducted, with each experiment performed in duplicate to ensure accuracy for statistical modelling purposes. The responses from these experiments are summarized in Table 2.

Table 1 Ranges and levels of variables that influenced the desulfurization process

	Range and levels		
Variables	−1	0	+1
Catalyst dosage (mg) (*A*)	50	70	90
Oxidant concentration (mL) (*B*)	3	5.5	8
Temperature (°C) (*C*)	40	55	70

As shown in the Table 2, the response values vary between 13.3 and 92.17, with a ratio of 6.93 between the maximum and minimum values, indicating that no value transformation was required.

3.7.1. Analysis of parametric conversion of DBT in model fuel. A second-order polynomial can be used to approximate the mathematical correlation between the three variables and the response (eqn (2)).

$$\text{Response } (R) = 31.66 - 8.67A - 0.4825B + 6.63C - 6.67AB - 2.64AC + 21.67BC - 14.97A^2 + 11.49B^2 + 22.47C^2. \quad (2)$$

The above-mentioned equation relies on a quadratic model recommended by the software, which performed well than other models *i.e.*, linear, cubic, and 2-factor interactions (2FI) in terms of fitting the experimental data effectively.

The lack of fit test (Table 3) assesses the difference between residual error and pure replication error and provides the Fisher's test value (*F*-value) for all the models. For a model to be considered significant, its *F*-value must be lower.[42] The results of the Fisher's test revealed that the calculated *F*-value exceeded the tabulated *F*-value for the corresponding degrees of freedom, leading to the rejection of the null hypothesis of a "significant lack of fit" for the linear, 2FI, and quadratic models. This

Table 2 ANOVA results for the ODS process

	Factor 1	Factor 2	Factor 3	Response
Run order	*A*: catalyst dosage (mg)	*B*: oxidant conc. (mL)	*C*: temperature (°C)	R^1 (%)
1	70	5.5	55	30.64
2	50	8	55	43.1
3	70	8	70	92.17
4	70	3	70	50.8
5	70	5.5	55	32.1
6	70	5.5	55	32.23
7	70	8	40	37.1
8	90	5.5	40	25.3
9	50	5.5	70	58.3
10	90	5.5	70	34.8
11	90	8	55	13.3
12	90	3	55	26.6
13	70	3	40	82.4
14	50	5.5	40	38.23
15	50	3	55	29.73

Table 3 Lack of fit test

Source	Sum of squares	df	Mean square	*F*-value	*p*-Value	
Linear	5439.29	9	604.37	775.39	0.0013	
2FI	3355.61	6	559.27	717.53	0.0014	
Quadratic	**8.18**	**3**	**2.73**	**3.50**	**0.2302**	**Suggested**
Cubic	0.0000	0				**Aliased**
Pure error	1.56	2	0.7794			

Table 4 Model summary statistics

Source	Std. dev.	R^2	Adjusted R^2	Predicted R^2	
Linear	22.24	0.1493	−0.0827	−0.7738	
2FI	20.49	0.4751	0.0814	−1.5933	
Quadratic	**1.40**	**0.9985**	**0.9957**	**0.9790**	**Suggested**
Cubic	0.8829	0.9998	0.9983		**Aliased**

indicates that the lack of fit is not significant. Among these models, the quadratic model, which is of higher polynomial order, was chosen. When considering model summary statistics for model selection, except for the aliased model, the quadratic model emerges as the best choice due to its low standard deviation and high R-squared statistics (as shown in Table 4).

3.7.2. Statistical significance assessment of the quadratic model using ANOVA. Table 5 presents the results from evaluating the quadratic response surface model, where the variability and associated degrees of freedom are calculated for the model's components, facilitating the computation of the mean square values.[43]

With an *F*-value of 364.20, the model demonstrates a high level of significance. The likelihood of observing such an *F*-value due to random variation is merely 0.01%.

p-Values below 0.05 suggest that the model terms are statistically significant, with terms *A*, *C*, *AB*, *AC*, *BC*, A^2, B^2, and C^2 identified as significant.[42] In contrast, values above 0.1 indicate that the corresponding terms do not show significant effects. The lack of fit *F*-value of 3.50 (Table 3) suggests that the lack of fit is not significant relative to pure error, with a 23.02% likelihood of observing such an *F*-value due to chance. The predicted R^2 value of 0.9790 is very close to the adjusted R^2 of 0.9957, with a difference of under 0.2 (Table 4). Adequate precision, which measures the signal-to-noise ratio, should ideally exceed 4; the ratio for the current model is 71.135, indicating a robust signal-to-noise ratio.

Fig. 6(a) illustrates a graphical comparison between experimental and predicted DBT conversion percentages, showing close alignment between the experimental data points and the regression line of predicted values, indicating minimal divergence. In Fig. 6(b), the dispersion of random residuals along the line correlating run number with internally studentized residuals suggests the model's accuracy. Fig. 6(c), depicting the plot of internally studentized residuals against normal percent probability, demonstrates an even distribution of model terms, confirming the adequacy of the regression model.

3.7.3. Response surface analysis. Two-dimensional contour plots were created using response surface methodology (RSM)[44] to analyze the interaction of two variables, with the third variable held constant. This analysis evaluated the interrelationship among the three factors: catalyst dosage, oxidant ratio, and temperature, which impact the desulfurization rate. Additionally, three-dimensional response surface plots were created to illustrate the interaction effects on the desulfurization rate, considering all three factors simultaneously.[45] Fig. 7(a)–(f) demonstrates the impact of varying catalyst dosage, oxidant ratio, and temperature on the rate of desulfurization.

Notably, increasing the oxidant ratio resulted in an increase in desulfurization efficiency, suggesting that 8 mL is the

Table 5 Results of ANOVA for the quadratic model

Source	Sum of squares	df[a]	Mean square	*F*-value	*p*-Value	
Model	6385.97	9	709.55	364.20	<0.0001	Significant
A-catalyst dosage	601.35	1	601.35	308.66	<0.0001	
B-oxidant conc.	1.86	1	1.86	0.9559	0.3731	
C-temperature	351.66	1	351.66	180.50	<0.0001	
AB	177.82	1	177.82	91.27	0.0002	
AC	27.93	1	27.93	14.34	0.0128	
BC	1877.92	1	1877.92	963.89	<0.0001	
A^2	827.13	1	827.13	424.54	<0.0001	
B^2	487.71	1	487.71	250.33	<0.0001	
C^2	1863.90	1	1863.90	956.70	<0.0001	
Residual	9.74	5	1.95			
Lack of fit	8.18	3	2.73	3.50	0.2302	Not significant
Pure error	1.56	2	0.7794			
Cor total[b]	6395.71	14				

[a] df = degree of freedom. [b] Cor total = amount of variation around the mean of the observations.

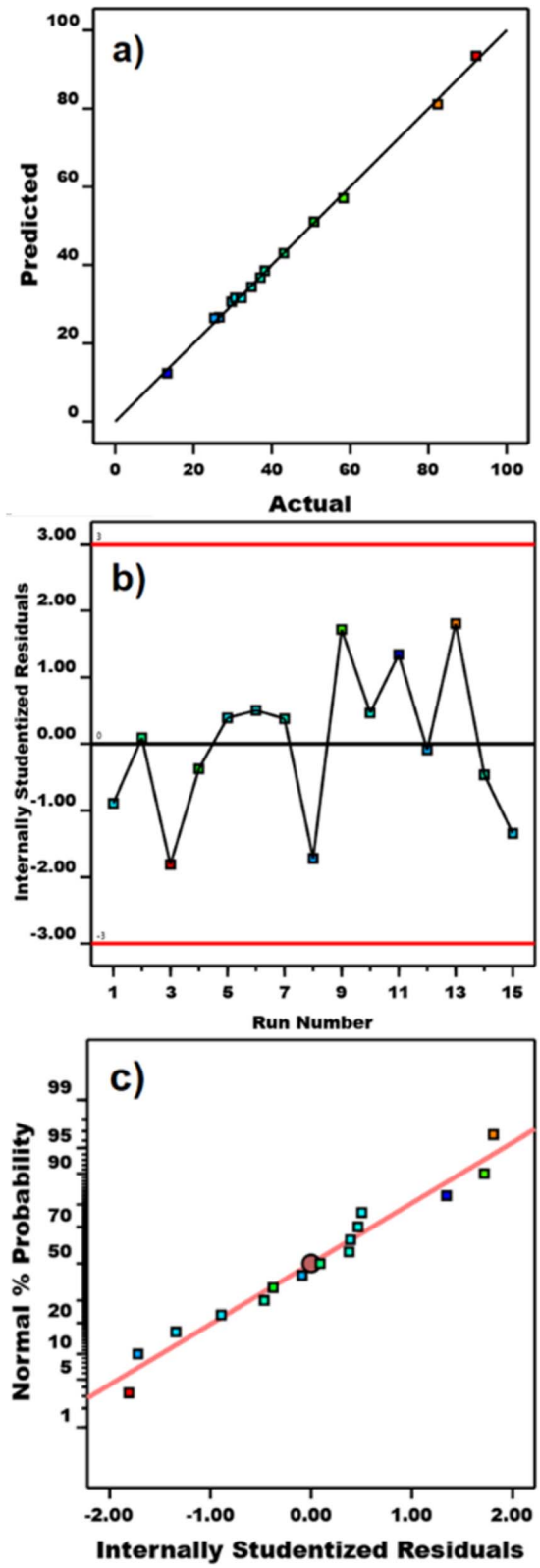

Fig. 6 (a) Predicted *vs.* actual responses of DBT conversion, (b) internally studentized against the run number, and (c) normal % probability *vs.* internally studentized residuals.

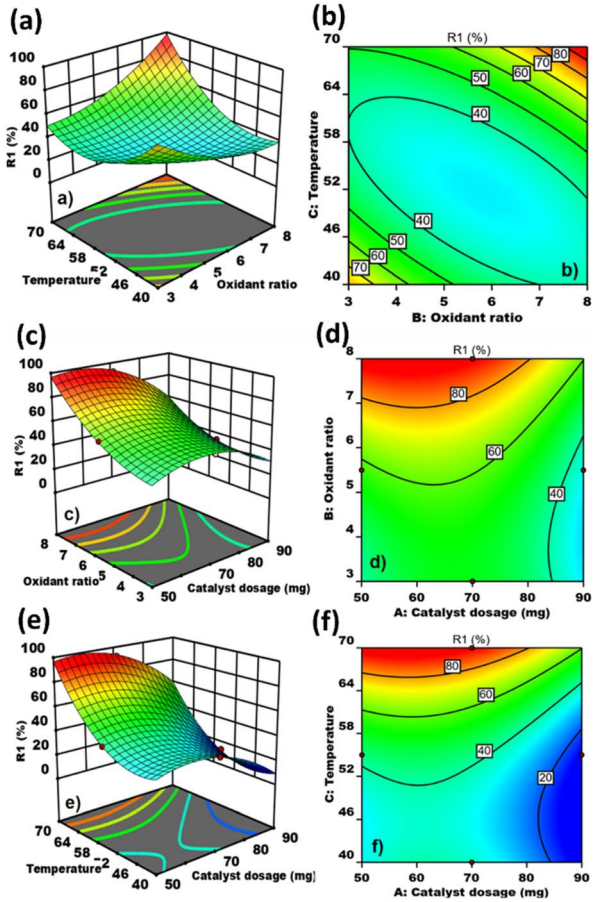

Fig. 7 Contour plots and 3D graphs illustrating: (a and b) the effect of temperature and oxidant concentration, (c and d) the effect of oxidant concentration and catalyst dosage, and (e and f) the effect of temperature and catalyst dosage.

optimal concentration of oxidant for achieving significant enhancement of sulfur removal. The oxidant ratio and temperature exhibit a linear relationship (Fig. 7(a)). The desulfurization rate initially declined between 40 and 60 °C; however, from 60 to 70 °C, the desulfurization rate significantly increased, indicating that 70–75 °C is the optimal temperature for the ODS process. Similarly, the contour plot indicates that the maximum desulfurization rate was achieved with an oxidant ratio of 8 mL and at a temperature of 70 °C (Fig. 7(b)).

Furthermore, the impact of catalyst dosage and oxidant concentration on the desulfurization of model fuel oil has also been examined. This was visualized and evaluated using three-dimensional response surface and contour plots (Fig. 7(c) and (d)). These figures demonstrate that increasing the oxidant ratio led to a steady and significant rise in sulfur removal from the model fuel oil, consistent with the observations in Fig. 7(a) and (b). The desulfurization rate significantly increased as the catalyst dosage was raised from 50 to 70 mg (Fig. 7(c)). However, further increasing the catalyst dosage from 70 to 90 mg resulted

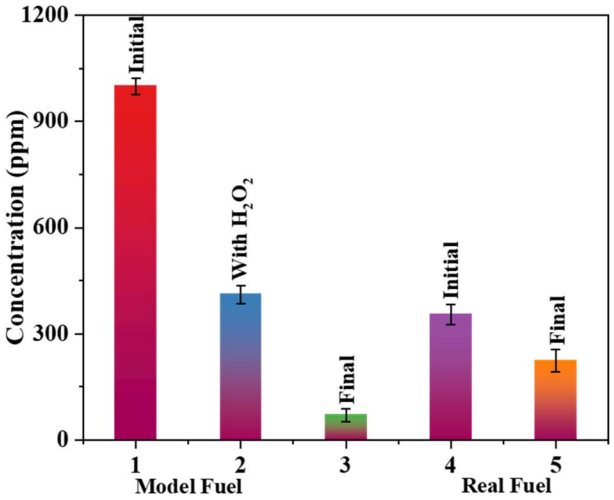

Fig. 8 Comparison of DBT conversion in model fuel and real fuel.

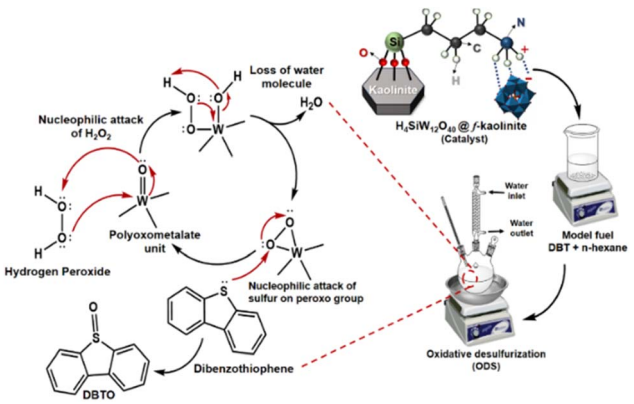

Fig. 9 Proposed mechanism for the conversion of DBT in the oxidative desulfurization process using $H_4SiW_{12}O_{40}$@f-kaolinite.

in a decrease in the desulfurization rate. Similarly, the contour plot indicates that the highest desulfurization rate was achieved with a catalyst dosage between 70 and 75 mg and an oxidant ratio of 8 mL (Fig. 7(d)). These results demonstrate that the optimal catalyst dosage is between 70 and 75 mg. Beyond this range, any further increase in the catalyst amount negatively impacts the desulfurization process, likely due to catalyst agglomeration. Additionally, the results indicate a direct proportional relationship between the catalyst amount and the oxidant ratio.

Similarly, a direct relationship was observed between the catalyst dosage and temperature, as illustrated in Fig. 7(e) and (f). The highest desulfurization efficiency was achieved within a temperature range of 60–70 °C and with a catalyst dosage of 70–75 mg, further validating the optimal conditions for both temperature and catalyst dosage.

3.8. Investigating DBT conversion in the real fuel sample

A real fuel sample was collected from a regional petrol pump and subjected to the ODS process under conditions similar to those applied to the model fuel oil. The DBT concentration in the real fuel decreased from 354 ppm to 224 ppm, which is lower than the reduction observed in the model oil. This decline in oxidative desulfurization efficiency is attributed to the complex composition, presence of contaminants and impurities, and the inclusion of additives in the real fuel. The DBT conversion in both model and real fuels is illustrated in Fig. 8.

3.9. Proposed mechanism

A reaction mechanism for oxidative desulfurization using $H_4SiW_{12}O_{40}$@f-kaolinite is shown in Fig. 9. The mechanism involves the nucleophilic attack of hydrogen peroxide on the tungsten–terminal oxygen (W=O), leading to the formation of anionic polyperoxometalate. Subsequently, the nucleophilic attack of the sulfur content in dibenzothiophene on the peroxo group results in the formation of sulfoxide, with the anionic species being regenerated into the original polyoxometalate unit ($[PW_{12}O_{40}]^{3-}$) by reduction.

Table 6 Comparison of the current system with the other reported systems

No.	Catalyst	Sulfur content	Reaction conditions	Efficiency	References
1	Superhydrophobic magnetic carbon composite catalyst MoOx/MC-600	200 mg kg^{-1}	O_2 (oxidant), 120 °C, 6 h	99.9%	46
2	Europium Lindqvist encapsulated into the nanoporous ZIF-8 support (EuW_{10}@ZIF-8)	1500 ppm	3 h, 70 °C	96%	47
3	Hollow PW_{12}/TiO_2@$MgCO_3$	350 ppm	80 g dose, 25 °C, 100 min, 5.5 oxidant/sulfur ratio	95.3%	48
4	Polyoxometalate based hybrids, $[H_2TPP]$ $[K_5BVW_{11}O_{40}]\cdot 2CH_3CN\cdot 2H_2O$	200 ppm	60 °C, 2 h	~99.5%	49
5	Vanadium-substituted Dawson-type polyoxometalate $[cetrimonium]_{11}P_2W_{13}V_5O_{62}$	500 ppm	7.5 g L^{-1} catalyst, O/S mole ratio 8, 70 °C, 45 min	94	50
6	POM supported on functionalized metakaolinite $CoMo_6$/MKA-F catalyst	1 mmol of diphenyl sulfide	80 °C, 50 mg catalyst, 5.0 mL of acetonitrile, 1.0 mL of H_2O_2	90%	34
7	$H_4SiW_{12}O_{40}$@f-kaolinite	1000 ppm	70 °C, 70 mg catalyst dosage, 8 mL of oxidant	92.17%	This study

3.10. Comparison of sulfur removal efficiency in various catalytic systems

Functionalization with APTES incorporates amine groups that greatly enhance the dispersion of POMs, thereby increasing the availability of active sites. The strong interaction between POMs and the functionalized kaolinite ensures that the catalyst remains reusable with minimal loss of activity over multiple cycles. Additionally, APTES and kaolinite are both cost-effective and readily available. Their combination with POMs results in a more economical catalyst compared to noble metal-based or other high-cost alternatives used for oxidative desulfurization (ODS). Table 6 indicates that achieving a sulfur removal efficiency exceeding 90% in the previously reported studies necessitated elevated temperatures and prolonged reaction durations. Our system exhibits superior performance. Remarkable conversion efficiency of 92.17% within 18 minutes, at 70 °C, an oxidant concentration of 8 ml against pm concentration, underscores the enhanced efficacy and efficiency of our system in comparison to existing methodologies.

3.11. Recyclability of $H_4SiW_{12}O_{40}$@f-kaolinite catalyst

The recyclability of catalysts offers various benefits, including cost-effectiveness, minimizing environmental impact through waste reduction, conserving valuable resources, contributing to process stability, and improving overall process economics by extending catalyst lifespan and enhancing efficiency in industrial operations. To evaluate the recyclability of $H_4SiW_{12}O_{40}$@f-kaolinite, the upper layer from the biphasic reaction system, following oxidative desulfurization, was separated using a separating funnel. The lower layer was then employed for the next ODS cycle under similar reaction conditions by introducing the model oil and fresh hydrogen peroxide. As shown in Fig. 10, the catalyst could be recycled over five cycles without any significant loss in efficiency.

3.12. Stability assessment of recycled $H_4SiW_{12}O_{40}$@f-kaolinite catalyst

To assess the stability of $H_4SiW_{12}O_{40}$@f-kaolinite, the recycled catalyst was analyzed using FT-IR, as depicted in Fig. 11. The results indicate that the catalyst preserved its initial elemental structure, as there is no notable difference in the spectra between the fresh and recycled catalyst.

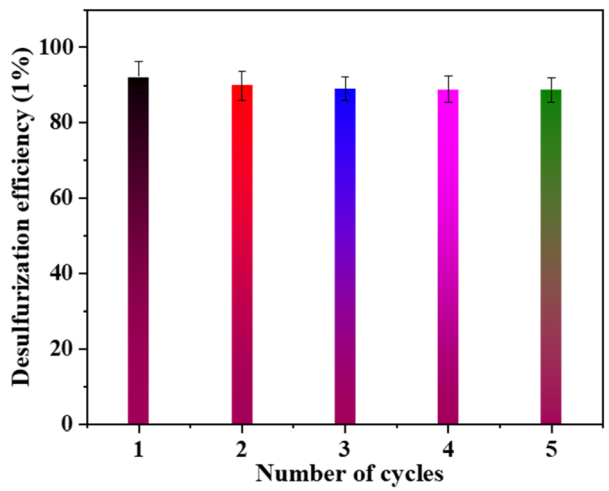

Fig. 10 Recyclability of $H_4SiW_{12}O_{40}$@f-kaolinite over five cycles under optimum conditions.

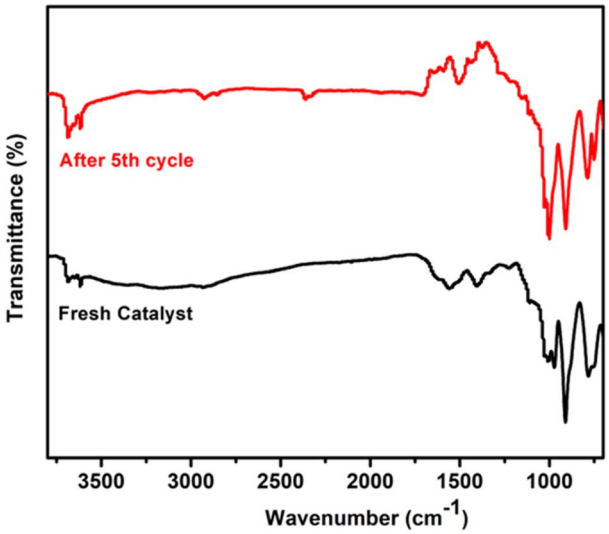

Fig. 11 FT-IR spectra of fresh and recycled catalyst.

4 Conclusions

The catalytic performance of the facile, robust, efficient, and environmentally sustainable catalyst $H_4SiW_{12}O_{40}$@f-kaolinite for the oxidative desulfurization (ODS) of dibenzothiophene (DBT) has been investigated in both model and real fuel samples. The catalyst was synthesized by functionalizing kaolinite and then immobilizing polyoxometalates on the surface of f-kaolinite. To optimize sulfur conversion, a three-level Box–Behnken design of experiments was employed to study the influence of three independent variables: catalyst dosage, oxidant concentration, and reaction temperature. The maximum DBT reduction, recorded at the optimal conditions of 70 mg catalyst dosage, 8 mL oxidant concentration, and 70 °C, was 78.3 ppm with a conversion rate of 92.2%. The results from ANOVA analysis indicate a significant quadratic model with an R^2 value of 0.99 and an insignificant lack of fit with an F-value of 3.50. In the real fuel sample, the DBT content was reduced from 354 ppm to 224.8 ppm, which is lower than that in the model fuel. This decrease in conversion rate is attributed to the complex composition, presence of contaminants and impurities, and additives in the real fuel. While the catalyst has shown potential for recycling up to five cycles while maintaining its elemental composition, suggesting that $H_4SiW_{12}O_{40}$@f-kaolinite could be a candidate for industrial applications, it is important to note that the current study's scale is limited. Therefore, a more cautious approach is warranted. Further research, including larger-scale experiments and scaling-up studies, is essential to fully evaluate the catalyst's industrial viability.

Data availability

All data supporting the findings of this study are included within the manuscript.

Author contributions

Conceptualization, Toheed Akhter and Sadaf Ul Hassan; methodology, Hamna Khalid; validation, Arsheen Umar, Muhammad Shahid Nazir, Muhammad Asim Farid, Chan Ho Park, and Zulfiqar Ali; formal analysis, Hamna Khalid; investigation, Hamna Khalid and Sadaf Ul Hassan; resources, Toheed Akhter, Sadaf Ul Hassan, Asif Mahmood and Waheed Al-Masry; writing – original draft preparation, Toheed Akhter and Sadaf Ul Hassan; writing – review and editing, Toheed Akhter; supervision, Toheed Akhter and Sadaf Ul Hassan; all authors have read and agreed to the published version of the manuscript.

Conflicts of interest

The authors declare that there are no conflicts of interest.

Acknowledgements

The authors are thankful to the Department of Chemistry, Chemical Engineering and Interdisciplinary Research Centre in Biomedical Materials (IRCBM) Center at COMSATS University, Islamabad, Lahore Campus for providing the facilities of resources and samples characterizations. This work was also supported by the National Research Foundation of Korea (NRF) grant funded by the Korea government (MSIT) (No. RS-2024-00408370). The authors also acknowledge the funding provided by Researcher's Supporting Project Number (RSP2024R43), King Saud University, Riyadh, Saudi Arabia.

References

1 M. Ja'fari, S. L. Ebrahimi and M. R. Khosravi-Nikou, *Ultrason. Sonochem.*, 2018, **40**, 955–968.
2 A. Rajendran, T.-y. Cui, H.-x. Fan, Z.-f. Yang, J. Feng and W.-y. Li, *J. Mater. Chem. A*, 2020, **8**, 2246–2285.
3 V. C. Srivastava, *RSC Adv.*, 2012, **2**, 759–783.
4 F. Boshagh, M. Rahmani, K. Rostami and M. Yousefifar, *Energy Fuels*, 2021, **36**, 98–132.
5 S. Houda, C. Lancelot, P. Blanchard, L. Poinel and C. Lamonier, *Catalysts*, 2018, **8**, 344.
6 M. Stylianou, I. Vyrides and A. Agapiou, *J. Chromatogr. B*, 2021, **1171**, 122602.
7 R. Y. Mamuad and A. E. S. Choi, *Energies*, 2023, **16**, 2738.
8 M. G. T. Alcaraz, A. E. S. Choi, N. P. Dugos and M.-W. Wan, *Chem. Eng. Trans.*, 2023, **103**, 553–558.
9 M. M. Haboc, N. P. Dugos, A. E. S. Choi and M.-W. Wan, *Chem. Eng. Trans.*, 2023, **103**, 559–564.
10 J. Xu, S. Zhao, W. Chen, M. Wang and Y.-F. Song, *Chem.–Eur. J.*, 2012, **18**, 4775–4781.
11 L. Chen, J.-T. Ren and Z.-Y. Yuan, *Appl. Catal., B*, 2022, **305**, 121044.
12 A. Mortezaee, S. Movahedirad and M. A. Sobati, *Can. J. Chem. Eng.*, 2023, **101**, 1802–1814.
13 M. Safa, B. Mokhtarani, H. R. Mortaheb, K. Tabar Heidar, A. Sharifi and M. Mirzaei, *Energy Fuels*, 2017, **31**, 10196–10205.
14 S. U. Hassan, S. Shafique, B. A. Palvasha, M. H. Saeed, S. A. R. Naqvi, S. Nadeem, S. Irfan, T. Akhter, A. L. Khan and M. S. Nazir, *Chemosphere*, 2023, **313**, 137418.
15 H. Khalid, A. Umar, M. H. Saeed, M. S. Nazir, T. Akhtar, A. Ikhlaq, Z. Ali and S. U. Hassan, *J. Ind. Eng. Chem.*, 2024, DOI: **10.1016/j.jiec.2024.06.043**.
16 M. T. Pope and A. Müller, *Angew. Chem., Int. Ed. Engl.*, 1991, **30**, 34–48.
17 F. Lefebvre, *Inorganics*, 2016, **4**, 13.
18 N. Parveen, A. A. Hanif, S. u. Hassan, A. Rehman, S. Razzaque, A. Mahmood, W. Al-Masry, T. Kim, S.-K. Han, C. H. Park, S. Nazir, Z. Ali and T. Akhter, *Polym. Compos.*, 2024, **45**(12), 10720–10733.
19 S. Karamat, T. Akhter, S. Ul Hassan, M. Faheem, A. Mahmood, W. Al-Masry, S. Razzaque, S. Ashraf, T. Kim, S.-K. Han and C. H. Park, *J. Ind. Eng. Chem.*, 2024, **137**, 503–513.
20 M. Maqbool, N. Parveen, S. Jaffar, S. U. Hassan, A. Mahmood, W. Al-Masry, T. Kim, S.-K. Han, C. H. Park, S. Razzaque and T. Akhter, *Chem.–Asian J.*, 2024, **19**, e202400002.
21 S.-S. Wang and G.-Y. Yang, *Chem. Rev.*, 2015, **115**, 4893–4962.
22 N. Saikia, D. Bharali, P. Sengupta, D. Bordoloi, R. Goswamee, P. Saikia and P. Borthakur, *Appl. Clay Sci.*, 2003, **24**, 93–103.
23 M.-q. Jiang, X.-y. Jin, X.-Q. Lu and Z.-l. Chen, *Desalination*, 2010, **252**, 33–39.
24 N. Nabbou, M. Belhachemi, M. Boumelik, T. Merzougui, D. Lahcene, Y. Harek, A. A. Zorpas and M. Jeguirim, *C. R. Chim.*, 2019, **22**, 105–112.
25 H. Zhang, R. Zhao, Z. Liu, X. Zhang and C. Du, *Appl. Clay Sci.*, 2023, **231**, 106730.
26 S. Attique, M. Batool, M. Yaqub, O. Goerke, D. H. Gregory and A. T. Shah, *Waste Manage. Res.*, 2020, **38**, 689–695.
27 J. C. Miranda-Trevino and C. A. Coles, *Appl. Clay Sci.*, 2003, **23**, 133–139.
28 M. R. Abukhadra, B. M. Bakry, A. Adlii, S. M. Yakout and M. E. El-Zaidy, *J. Hazard. Mater.*, 2019, **374**, 296–308.
29 S. Rastegar Koohi, S. Allahyari, D. Kahforooshan, N. Rahemi and M. Tasbihi, *J. Inorg. Organomet. Polym. Mater.*, 2019, **29**, 365–377.
30 M. Raji and R. Bouhfid, *RSC Adv.*, 2020, **10**, 4916–4926.
31 G. K. Dedzo, *Isr. J. Chem.*, 2019, **59**, 778–788.
32 P. Anju and V. S. Prasad, *Langmuir*, 2020, **36**, 1761–1767.
33 H. Cheng, Y. Zhou and Q. Liu, in *Nanomaterials from Clay Minerals*, Elsevier, 2019, pp. 285–334.
34 M. Muñoz, M. A. Gallo, A. Gutiérrez-Alejandre, D. Gazzoli and C. I. Cabello, *Appl. Catal., B*, 2017, **219**, 683–692.
35 C. A. Vieira, B. F. Ferreira, A. F. da Silva, M. A. Vicente, R. Trujillano, V. Rives, K. J. Ciuffi, E. J. Nassar and E. H. de Faria, *ACS Appl. Nano Mater.*, 2018, **1**, 3867–3877.
36 Q. Zhang, Z. Yan, J. Ouyang, Y. Zhang, H. Yang and D. Chen, *Appl. Clay Sci.*, 2018, **157**, 283–290.
37 É. Makó, Z. Sarkadi, Z. Ható and T. Kristóf, *Appl. Clay Sci.*, 2023, **231**, 106753.
38 I. Fatimah, *J. King Saud Univ., Sci.*, 2018, **30**, 250–257.

39 M. J. da Silva, P. H. da Silva Andrade, T. A. Silva, M. B. T. Diniz, S. O. Ferreira, R. C. da Silva and E. N. D. de Araujo, *Catal. Lett.*, 2024, **154**, 1648–1663.
40 M. Liberka, M. Zychowicz, J. Hooper, K. Nakabayashi, S.-i. Ohkoshi and S. Chorazy, *Angew. Chem., Int. Ed.*, 2023, **62**, e202308284.
41 O. J. Curnow and R. Senthooran, *Polyhedron*, 2023, **233**, 116318.
42 I. Afzal, T. Akhter, S. U. Hassan, H. K. Lee, S. Razzaque, A. Mahmood, W. Al-Masry, H. Lee and C. H. Park, *ACS ES&T Water*, 2024, **4**, 648–660.
43 A. E. S. Choi, S. A. Roces, N. P. Dugos and M. W. Wan, *J. Cleaner Prod.*, 2022, **363**, 132357.
44 G. R. H. Barilla, C. A. W. Chen, M. Z. M. Valencia, N. P. Dugos and A. E. S. Choi, *S. Afr. J. Chem. Eng.*, 2022, **42**, 61–71.
45 A. E. S. Choi, S. A. Roces, N. P. Dugos and M. W. Wan, *Comput. Chem. Eng.*, 2022, **166**, 107965.
46 W. Jiang, J. Xiao, L. Dong, C. Wang, H. Li, Y. Luo, W. Zhu and H. Li, *ACS Sustain. Chem. Eng.*, 2019, **7**, 15755–15761.
47 M. Sun, R. Abazari, J. Chen, C. M. Hussain, Y. Zhou and A. M. Kirillov, *ACS Appl. Mater. Interfaces*, 2023, **15**, 52581–52592.
48 S. U. Hassan, H. Khalid, S. Shafique, M. A. Farid, M. H. Saeed, Z. Ali, M. S. Nazir, M. Hussain and Y.-K. Park, *Chemosphere*, 2023, **339**, 139662.
49 S. U. Hassan, S. Ahmad, M. A. Farid, S. Nadeem, Z. Ali, R. Abro, A. Mohyuddin, M. S. Nazir, M. Hussain and Y.-K. Park, *J. Ind. Eng. Chem.*, 2022, **116**, 438–446.
50 F. Banisharif, M. R. Dehghani, M. C. Capel-Sanchez and J. M. Campos-Martin, *J. Ind. Eng. Chem.*, 2017, **47**, 348–359.